Chemical Science

ROYAL SOCIETY OF CHEMISTRY

EDGE ARTICLE

View Article Online
View Journal | View Issue

Cite this: *Chem. Sci.*, 2026, **17**, 2233

All publication charges for this article have been paid for by the Royal Society of Chemistry

Received 11th September 2025
Accepted 24th November 2025

DOI: 10.1039/d5sc07016c

rsc.li/chemical-science

Chiral poly(aza-norbornene) derivatives with tunable tacticity and living ROMP capability

Jing Bai,[ab] Yu Wang,*[a] Yisong Wang,[c] Na Zhang,[ab] Xiaoyang Wang,[a] Yan Xu*[c] and Wei You*[ab]

Ring-opening metathesis polymerization (ROMP) is a powerful tool to produce various polymers with diverse structures and functions, but its tacticity controllability, especially for enantio-pure monomers, is relatively unexplored. The challenge lies in both the difficulty of achieving chiral monomers and the control of head/tail regioselectivity during ROMP. We herein report the synthesis and application of a sulfonamide derivative of commercial chiral Vince lactam. The easily available monomer showed simultaneous living ROMP capability and tunable head/tail regioselectivity with commercial Ru-based catalysts. More specifically, the use of the Grubbs' III catalyst (Ru-3) gave rise to head-to-tail regioselectivity, leading to isotactic "living" polymers. In contrast, the use of cyclometalated Ru-based catalysts (Ru-4 and Ru-5) enabled the formation of head-to-head polymers, leading to syndiotactic polymers. Detailed experimental and DFT studies suggest that the regioselectivity is dominated by the chain-end-control mechanism. The precise microstructural tunability enables us to systematically investigate thermal properties, crystallinity, and dielectric properties of the hydrogenated ROMP polymers.

Introduction

Tacticity significantly influences polymer properties, including thermal behavior, crystallinity, mechanical strength, and dielectric performance.[1–5] In conventional vinyl-addition polymerization, well-defined tacticity (*i.e.*, isotactic or syndiotactic) is achieved using prochiral vinyl monomers and stereo-controlled catalysts. Alternatively, ring-opening polymerization (ROP) enables the incorporation of stereocenters *via* cyclic chiral monomers. During ROP, the inherent chirality of monomers is directly translated into polymer tacticity, thereby expanding the diversity of backbone chirality in synthetic polymers.

Ring-opening metathesis polymerization (ROMP) is a unique type of ROP that employs olefin metathesis reactions for ring-opening.[6,7] ROMP offers advantages including broad functional group tolerance[1,8,9] and living polymerization characteristics for precise structural control.[10–13] While monomer diversity, *cis*/*trans*-stereoselectivity, and head/tail-regioselectivity have been extensively explored in ROMP,[14–19] the studies about tacticity control are mostly limited to symmetric monomers.[20] For example, the pioneer work by Schrock,[21,22] Grubbs,[23] Ivin,[24] Rooney,[25] Delaude,[26] and Noels[27] *et al.* systematically studied the tacticity and *cis*/*trans*-selectivity control for monomers like norbornene, norbornadiene, 7-oxanorbornene, *exo*,*exo*-2,3-dicarbomethoxy-5-norbornene, and cyclopropene derivatives, but only a few chiral norbornene derivatives were investigated (Scheme 1).[28,29] This is mostly because for normal norbornene derivatives, it is extremely challenging to isolate or selectively synthesize a single enantiomer out of at least four possible *R*/*S* and *endo*/*exo*-isomers.[27] For chiral norbornene monomers, as the influence of *cis*/*trans*-selectivity can be eliminated upon backbone hydrogenation, tacticity is governed by both monomer chirality and head/tail regioselectivity (Scheme 1a).[20,28,30] For instance, even when using optically pure chiral monomers, poor head/tail regioselectivity can result in atactic polymers, leading to a waste of chirality. In comparison to Ru-based catalysts, Mo- and W-based catalysts are more prevalent for tacticity control in ROMP, likely due to the high rotational barriers of their carbene species, which provide the steric constraints necessary for stereo-control during polymerization.[31,32] However, the air and moisture sensitivity issues of Mo- and W-based carbene catalysts restrict their widespread application.[33–35]

There are a limited number of examples using chiral cyclic alkene monomers to produce isotactic polymers from Ru-catalyzed ROMP reactions (Scheme 1b). For example, Hillmyer and coworkers reported that chiral 3-substituted cyclooctene, synthesized through Pd-catalyzed kinetic resolution of allylic nucleophilic substitution, undergoes ROMP with high head-to-

[a]*Beijing National Laboratory for Molecular Sciences, CAS Key Laboratory of Engineering Plastics, Institute of Chemistry, Chinese Academy of Sciences, Beijing 100190, China. E-mail: weiyou@iccas.ac.cn; ywang507@iccas.ac.cn*

[b]*University of Chinese Academy of Sciences, Beijing 100049, China*

[c]*Beijing National Laboratory of Molecular Sciences (BNLMS), Key Laboratory of Bioorganic Chemistry and Molecular Engineering of Ministry of Education, College of Chemistry and Molecular Engineering, Peking University, Beijing 100871, China. E-mail: yanx@pku.edu.cn*

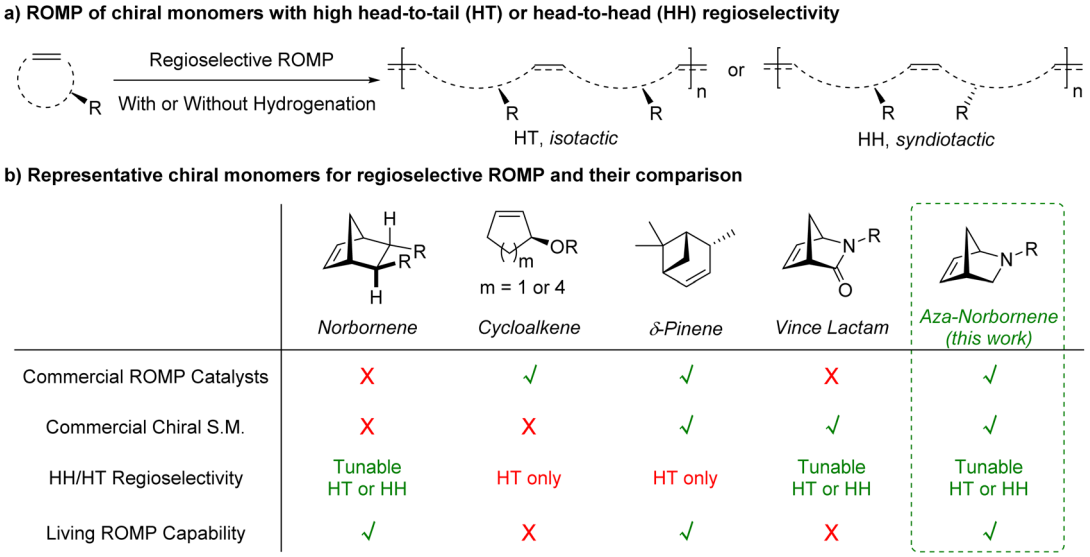

Scheme 1 (a) ROMP of chiral monomers with high HT or HH regioselectivity, leading to isotactic and syndiotactic polymers after hydrogenation, respectively. (b) Representative chiral monomers for regioselective ROMP and their comparison. Abbreviations: ROMP: ring-opening metathesis polymerization; HT: head-to-tail; HH: head-to-head; S. M.: starting material.

tail (HT) and *trans*-selectivity using the Grubbs second-generation catalyst (Ru-2 in Scheme 2). Subsequent hydrogenation yielded isotactic poly(ethylene-*co*-ethyl acetate) (EVA), exhibiting a substantially higher melting temperature (T_m) and crystallinity compared to commercial EVA produced by radical copolymerization.[36,37] Similar chiral polymers can also be made from chiral 3-substituted cyclopentene.[38] However, these polymerizations often exhibit broad molecular weight distributions due to chain transfer. More recently, δ-pinene, a bio-derived chiral monomer, has emerged as the only known monomer capable of achieving living polymerization with the Grubbs third-generation catalyst (Ru-3 in Scheme 2), while maintaining high *trans*- and HT-selectivity.[39] Nevertheless, its low ring strain ([3.1.1] bicyclic structure) and significant steric hindrance result in slow polymerization kinetics, and its copolymerization potential remains largely unexplored.

Notably, Vince lactam, a [2.2.1]-bicyclic strained alkene structurally analogous to norbornene, is commercially available in both enantiomeric forms as a key pharmaceutical reagent.[40] Its lactam moiety can be readily functionalized to generate chiral monomers suitable for ROMP. Buchmeiser and coworkers demonstrated that ROMP of (+)-Vince lactam and its derivatives proceeds with high regio- and stereoselectivity only when using Mo-, W-, or cyclometalated Ru-based initiators, whereas the use of Ru-3 yielded atactic polymers.[41] The authors revealed tunable regioselectivity, in which HT selectivity from

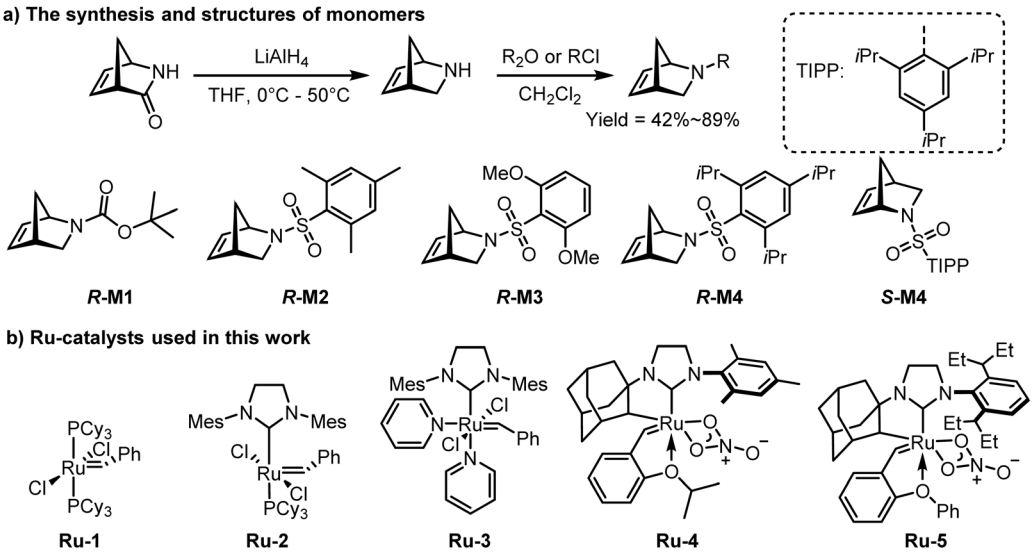

Scheme 2 (a) The synthesis and structures of monomers; (b) Ru-based catalysts used in this work.

Mo catalysts and head-to-head (HH) selectivity from W catalysts. However, the resulting polymers exhibit poor molecular weight control and inability for hydrogenation due to limited solubility (restricted to organic acids), and thus their microstructure–property relationships remain poorly understood. In this work, we present a two-step derivatization of Vince lactam to synthesize substituted chiral aza-norbornene monomers capable of living ROMP using commercially available Ru catalysts (Scheme 1b). Intriguingly, we observed tunable HT and HH regioselectivity from Ru-3 and cyclometalated Ru catalysts, respectively. Both experimental and density functional theory (DFT) calculations support a chain-end-control model for high regioselectivity.[42] This approach enables the synthesis of structurally precise polymers and provides a platform to systematically investigate how monomer functionality and catalyst selection dictate the microstructure. Moreover, the achieved stereocontrol allows for probing the effects of tacticity in these novel poly(aza-norbornene) derivatives on crystallization and dielectric properties post-hydrogenation.

Results and discussion

It is hypothesized that the carbonyl group in Vince lactam leads to unwanted chelation with catalysts, and thus, we first tried to move the carbonyl group out of the bicyclic structure. The commercial (−)-Vince lactam was reduced by lithium aluminum hydride ($LiAlH_4$) to yield a chiral secondary amine, which was then reacted with di-*tert*-butyl dicarbonate (Boc_2O) to synthesize a Boc-protected monomer, *tert*-butyl (1*R*,4*S*)-2-azabicyclo[2.2.1]hept-5-ene-2-carboxylate (abbreviated as *R*-M1), in a two-step reaction (Scheme 2a). Its polymerization was carried out using Ru-3 as the catalyst with a feeding ratio of *R*-M1 : Ru-3 = 500 : 1 in tetrahydrofuran (THF) as the solvent at 25 °C. However, the monomer conversion was unable to exceed 76%. Subsequently, we decided to replace the carbonyl group with a sulfonyl group, and a series of sulfonamide-substituted chiral aza-norbornene monomers were synthesized (*R*-M2, *R*-M3, and *R*-M4 in Scheme 2a).

The polymerization of monomers *R*-M2 and *R*-M3 with Ru-3 can be performed in dichloromethane (DCM), but the resulting polymers P-R2-Ru3 (represents the polymer made from *R*-M2 with Ru-3) and P-R3-Ru3 (represents the polymer made from *R*-M3 with Ru-3) were insoluble in THF. In contrast, the homopolymer from *R*-M4 with isopropyl groups (P-R4-Ru3) has good solubility in both DCM and THF, making it easier to be analyzed by gel permeation chromatography (GPC). It is speculated that the bulky isopropyl group reduced the π–π stacking interactions of the aromatic rings in the polymer, thereby increasing the polymer's solubility.[43] When the feeding ratio of *R*-M4 : Ru-3 was set to be 500 : 1, complete monomer conversion was achieved within 30 minutes. We then characterized the structure of the three corresponding polymers by nuclear magnetic resonance (NMR). As shown in Fig. S1, the polymer derived from the isopropyl-substituted *R*-M4 exhibited obviously clearer proton signals than the other two, indicating that the bulky substituent promotes a more ordered microstructure in the polymer, which is consistent with previous reports.[44,45] In summary, the bulky substituents on the sulfonamide monomers not only enhance the solubility of the polymer in solvents such as THF, but also facilitate the formation of a more regular microstructure in the polymer.

The homopolymerization of *R*-M4 initiated by various Ru catalysts (Scheme 2b) was then systematically investigated. The monomer-to-initiator ratio was set at 500 : 1 for Ru-1, Ru-2, and Ru-3, while a ratio of 50 : 1 was employed for the cyclometalated Ru catalysts, Ru-4 (commercially available) and Ru-5 (prepared according to the literature[46]). We found that the ^{1}H NMR spectra of the polymers P-R4-Ru2 and P-R4-Ru3, initiated by Ru-2 and Ru-3, were nearly identical (Fig. 1), while the ^{1}H NMR spectra of the polymers obtained with the cyclometalated Ru catalysts (Ru-4 and Ru-5) were completely different (Fig. 1). Although the chemical shifts of the olefinic protons (δ = 5.4–5.0 ppm) in all polymers were similar, only the polymers obtained with Ru-1, Ru-2, and Ru-3 exhibited peaks at δ = 4.82 ppm, 3.22 ppm, 2.37 ppm, and 1.44 ppm (highlighted in red in Fig. 1), while only the polymers obtained with Ru-1, Ru-4, and Ru-5 showed peaks at δ = 4.28 ppm and 1.97 ppm (highlighted in blue in Fig. 1). Products from Ru-4 and Ru-5 also had peaks around 2.98 ppm. The corresponding ^{13}C NMR spectra (Fig. S2) further revealed distinct chemical shifts between the polymers P-R4-Ru3 and P-R4-Ru5. P-R4-Ru3 lacked a peak at δ = 60.0 ppm, proving that the structures of the polymers obtained with Ru-2/Ru-3 and Ru-5 are completely different. The polymer P-R4-Ru1 initiated by Ru-1 displayed NMR peaks corresponding to both of the aforementioned P-R4-Ru3 and P-R4-Ru5, confirming that it likely contained the complicated sequence of HT and HH–TT connections and *cis*/*trans*-isomers. More interestingly, although P-R4-Ru3 and P-R4-Ru5 were polymerized from the same optically pure monomer *R*-M4, their optical rotation values were opposite. The specific rotation of P-R4-Ru3 was determined to be +30° mL g^{-1} dm^{-1} (5 mg mL^{-1} in chloroform), while that of P-R4-Ru5 was −29° mL g^{-1} dm^{-1}. This further confirms the structural differences between P-R4-Ru3 and P-R4-Ru5.

In order to illustrate the potential head-/tail-based regioisomers and *cis*-/*trans*-based stereoisomers, we further analyzed the structures of P-R4-Ru3 and P-R4-Ru5 by two-

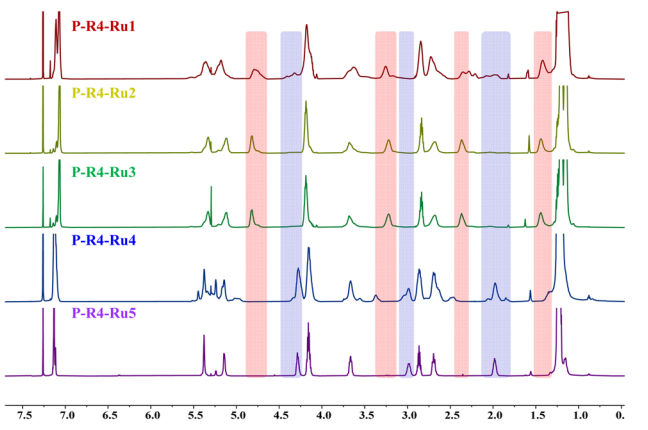

Fig. 1 ^{1}H NMR spectra of P-R4-Ru1, P-R4-Ru2, P-R4-Ru3, P-R4-Ru4, and P-R4-Ru5 (from top to bottom).

dimensional (2D)-NMR and Fourier transform infrared (FT-IR) spectroscopy to determine the precise structure of the polymers. ^{1}H–^{1}H COSY was used to determine whether there was any coupling of the protons on the backbone alkenes. If the alkenes in the main chain are HH/TT-connected, the two sets of alkenes are symmetric, thus showing only two separate signals. If the alkenes are HT-connected, the two protons on the olefin will show strong coupling. The ^{1}H–^{1}H COSY of P-R4-Ru3 (Fig. 2a) shows coupling of olefinic protons, confirming that P-R4-Ru3 is the HT product. The ^{1}H–^{1}H COSY of P-R4-Ru5 (Fig. 2b) shows no coupling of the protons on the olefin, indicating that the alkene is connected in the HH/TT manner. Based on the above analysis, we further hypothesize that the head-to-tail linkage in P-R4-Ru4 is identical to that in P-R4-Ru5, differing only in the *cis*/*trans* configuration. The ^{1}H–^{1}H COSY of P-R4-Ru4 (Fig. S41) shows no coupling of the olefinic protons, which confirms that the double bonds in P-R4-Ru4 are connected in the HH/TT manner. Moreover, based on the ^{1}H–^{1}H COSY and ^{1}H–^{13}C HSQC assignments of P-R4-Ru5 (Fig. S3), we observed that the peak at $\delta = 59.8$ ppm in the ^{13}C NMR corresponds to the methine carbon adjacent to the nitrogen, which is a distinct peak indicative of the HH/TT-connection (Fig. S2). Thus, based on the combined NMR analysis, P-R4-Ru2 and P-R4-Ru3 exhibited perfect HT regioselectivity, while the polymers obtained with Ru-4 and Ru-5 showed excellent HH/TT regioselectivity. Similar regioselectivity was achieved when changing the substrates to *R*-M2 and *R*-M3 (Fig. S48–S52). Although it is well-established that the cyclometalated Ru catalysts favor the formation of *cis*-alkenes during metathesis, this is the first time that their distinct ROMP head/tail regioselectivity has been observed in comparison to the Grubbs' series catalysts.

The next step is to reveal the olefin configuration in the polymer backbones. The peaks in the ^{1}H NMR spectrum of P-R4-Ru3 were assigned according to ^{1}H–^{1}H COSY. Oversaturation of the allylic protons was able to show the coupling constant of the olefinic protons to be around 10.2 Hz (Fig. S4), indicating *cis*-alkene configuration. However, in HH-polymer P-R4-Ru5, the two sets of olefinic protons do not couple, making it impossible to determine the alkene configuration from NMR analysis. As cyclometalated Ru-4 and Ru-5 are commonly used as *cis*-selective catalysts[23,30,47–49] and similar cyclometalated Ru catalysts have also been reported to produce *cis* products in the polymerization of Vince lactam derivatives,[41] we hypothesize that the alkenes in P-R4-Ru5 are mainly in the *cis* configuration. The *cis*-selectivity for the Ru-4 catalyst is poorer than that for Ru-5 according to their ^{1}H NMR comparison (Fig. 1). The FT-IR spectra of P-R4-Ru3, P-R4-Ru4, and P-R4-Ru5 were then compared (Fig. S5). Consistent with previous literature,[50–52] the *cis* and *trans* alkenes of polynorbornenes show clear differences in the FT-IR absorption near 700 cm^{-1}, confirming that the alkenes in P-R4-Ru3 and P-R4-Ru5 are primarily *cis*, while the absorption at 1026–949 cm^{-1} corresponds to a characteristic peak for the head-to-head/tail-to-tail linkage (Fig. S5).

In order to reveal why the two different types of Ru-based catalysts gave high but opposite head/tail regioselectivity, both model metathesis experiments and DFT calculations were performed. Regio- or stereo-selectivity control in chain-growth polymerization is usually achieved *via* two mechanisms: the chain-end-control (CEC) model, in which the last-inserted monomer determines the selectivity for the next insertion, and the enantiomorphic-site-control (ESC) model, in which the chirality of the catalyst determines the selectivity.[42] As none of the Ru-based catalysts used in this work is enantiomerically pure, it is more likely to be controlled through a CEC mechanism. Therefore, a ring-opening metathesis (ROM) model reaction was designed involving *R*-M4, 4-methoxystyrene, and

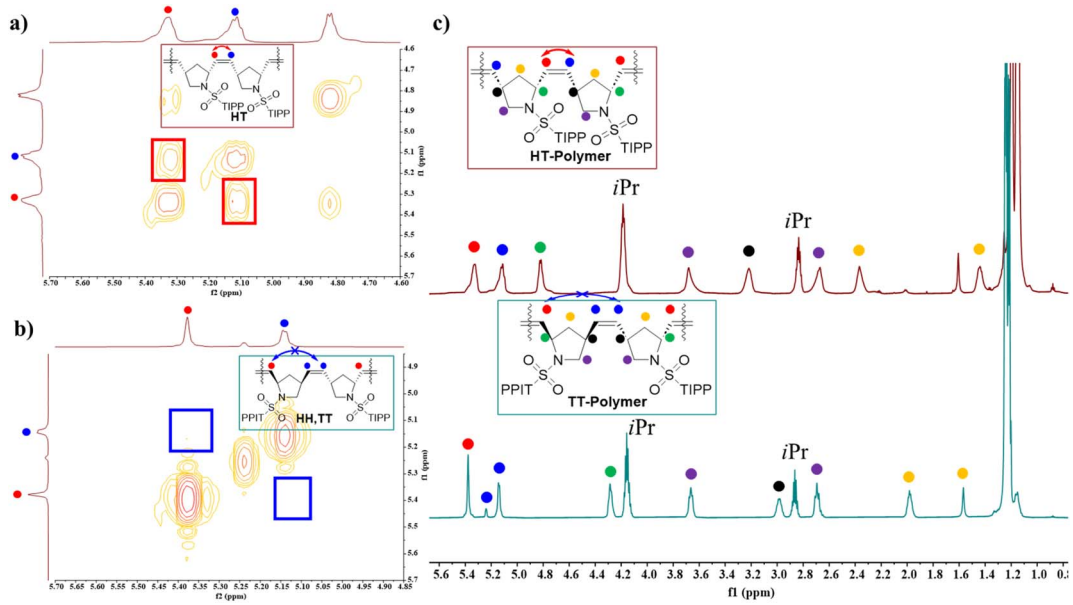

Fig. 2 (a) Partial zoom-in of ^{1}H–^{1}H COSY spectra of P-R4-Ru3 and (b) P-R4-Ru5 to show the distinct regioselectivity. (c) Stacked ^{1}H NMR spectra of P-R4-Ru3 (top) and P-R4-Ru5 (bottom) with peak assignments.

the Ru-3 catalyst. It is assumed that if the regioselectivity was controlled by the CEC mechanism, the ROM process would show no regioselectivity, and *vice versa*. The involvement of the methoxy group was to assist NMR peak assignment, and the results clearly showed that all four possible stereoisomers were produced in nearly identical amounts (Scheme 3a and Fig. S6). The DFT calculation for the first metathesis step also revealed similar energy barriers for all four isomers ($\Delta G^{\ddagger}$ = 12.4–15.1 kcal mol^{-1} calculated from Ru-3, Fig. S7 [53]), suggesting a non-selective metathesis when the carbene was connected with a phenyl group.

The energy barriers became significantly different when the carbene was changed to the ring-opened *R*-M4 (Scheme 3b left). The *cis*-configuration was selected as the representative model for downstream DFT calculations. When Ru-3 was connected with *R*-M4 through the head configuration (the nitrogen substituent is close to the carbene), the sequential cycloaddition favored the HT-connection over the HH-connection by $\Delta\Delta G^{\ddagger}$ = 6.8 kcal mol^{-1}. Similarly, if the initial Ru-3 connected with *R*-M4 *via* the tail (the nitrogen substituent is far from the carbene), the following TH-connection is favored by $\Delta\Delta G^{\ddagger}$ = 7.8 kcal mol^{-1} over the TT-connection (see Fig. S8 for more details). Therefore, no matter which regio-isomer is produced from the Ru-3-derived carbene, the incoming monomer will favor the formation of an HT-connection, which matches with the CEC mechanism. This is likely caused by the chiral environment around the Ru center after the chiral monomer insertion. In contrast, the cyclometalated ligands and the nitrate anions in Ru-4 catalysts promote the side-bound approach and the opposite HH–TT selectivity,[23,49,54,55] as HH is favored over HT by $\Delta\Delta G^{\ddagger}$ = 7.5 kcal mol^{-1}, and TT is favored over TH by $\Delta\Delta G^{\ddagger}$ = 7.2 kcal mol^{-1} (Scheme 3b, right and Fig. S9). All these trends are far beyond DFT prediction errors of relative barrier heights[56] and are perfectly consistent with the experimental results. It is noteworthy that the absolute values for the metathesis energy and barriers of ΔG and $\Delta G^{\ddagger}$ are all relatively low throughout the DFT calculation (<16 kcal mol^{-1}), which likely results from the high ring strain of the [2.2.1]-bicyclic *R*-M4 monomer and agrees well with the fast room-temperature ROMP that we experimentally observed.

Next, a systematic analysis of the homopolymerization of *R*-M4 under various conditions was conducted (Table 1). The calculation method of the *cis*-selective proportion in the polymer can be found in the SI (Fig. S10). When the feeding ratio of M : I was 500 : 1, the polymerization using catalyst Ru-1 was slower than that using Ru-2 and Ru-3 (Table 1, entries 1–3).

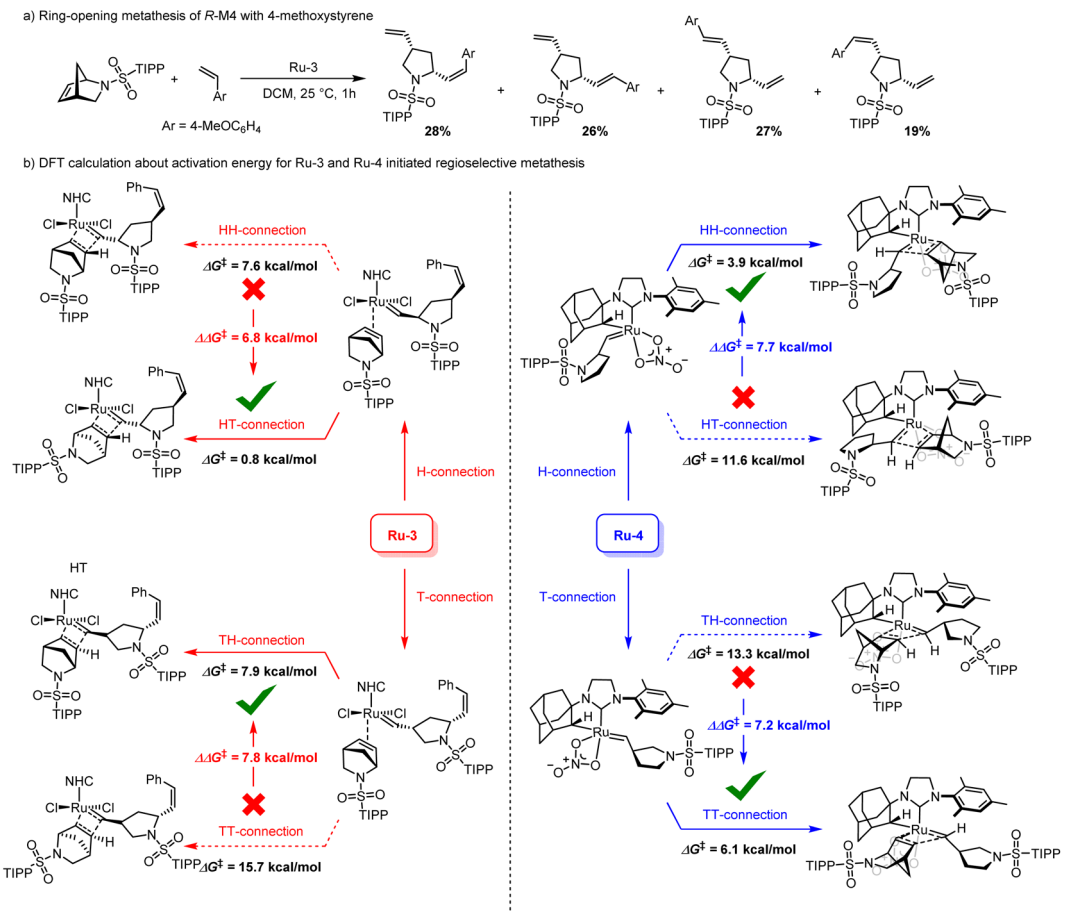

Scheme 3 (a) Ring-opening metathesis of *R*-M4 and 4-methoxystyrene; (b) DFT calculation for the Ru-3 and Ru-4 initiated regioselective metathesis. Free energies (kcal mol^{-1}) were obtained at the M06(D3)/def2 TVZPP/PCM(THF)//BP86(D3)/def2-SVP level. NHC = 1,3-di-mesitylimidazol-2-ylidene. See SI Fig. S7–S9 for more details.

Table 1 Homopolymerization conditions for the monomer *R*-M4[a]

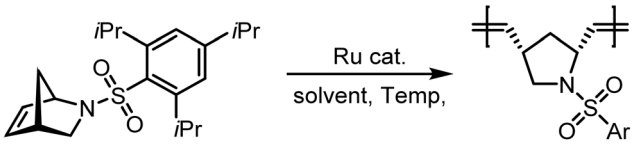

Entry	M : I	Catalyst	$[M]_0/M$	Solvent	Temp./°C	Time/h	$M_{n,theo}$ /kDa	M_n[b]/kDa	$Đ$[b]	Yield/%	*Cis*[c]%	HT/HH[d]
1	500 : 1	Ru-1	0.1	DCM	25	3	179.0	150.2	1.15	99	—	—
2	500 : 1	Ru-2	0.1	DCM	25	1	179.0	834.9	1.97	99	76	HT
3	500 : 1	Ru-3	0.1	DCM	25	0.5	179.0	231.2	1.03	99	76	HT
4	50 : 1	Ru-4	0.2	THF	25	12	17.9	213.3	2.40	99	—	HH
5	50 : 1	Ru-4	0.2	THF	0	12	17.9	436.1	2.21	99	—	HH
6	50 : 1	Ru-5	0.2	THF	25	12	17.9	103.9	2.68	99	85	HH
7	50 : 1	Ru-5	0.2	THF	0	24	13.9	179.3	2.42	77	93	HH
8	500 : 1	Ru-3	1.0	DCM	25	0.5	179.0	260.3	1.03	99	74	HT
9	500 : 1	Ru-3	0.1	DCM	40	0.5	179.0	253.0	1.04	99	75	HT
10	500 : 1	Ru-3	0.1	DCM	0	2	157.3	173.3	1.03	87	74	HT
11	500 : 1	Ru-3	0.1	THF	25	0.5	179.0	213.2	1.05	99	84	HT
12	500 : 1	Ru-3	0.1	THF	0	2	179.0	169.8	1.03	99	82	HT
13	500 : 1	Ru-3	0.1	Toluene	25	0.5	179.0	210.7	1.03	99	85	HT

[a] Reactions were run at a 0.1 mmol scale under an N_2 atmosphere. [b] Determined by GPC with a Refractive Index (RI) detector. [c] Determined by ^{1}H NMR analysis. See the SI (Fig. S10) for more details. When using Ru-1 and Ru-4, the ^{1}H NMR spectra of the polymers were too broad to enable accurate assignment or integration, so the numbers were not listed. [d] Determined by NMR analysis.

Although the selectivity of Ru-1 was poor, its molecular weight (M_n) and dispersity ($Đ$) were well-controlled. The polymer obtained with Ru-2 had a high molecular weight of 834.9 kDa and a broad molecular weight distribution ($Đ = 1.97$), likely due to incomplete initiation. The polymer produced with Ru-3 showed excellent molecular weight distribution control ($Đ = 1.03$). Despite the differences in M_n and $Đ$, the *cis*-selectivity and HT linkage of polymers from Ru-2 and Ru-3 were identical, demonstrating that the control of the polymer's regioselectivity likely depends on the N-heterocyclic carbene (NHC) ligand of the Ru catalyst. Solvent screening revealed that DCM gave the best molecular weight distribution control, but the lowest *cis*-selectivity (Table 1, entries 3, 11, and 13). In THF and toluene, the *cis*-selectivity reached ~85%. Lowering the reaction temperatures would slow down the propagation rates, while the reaction temperature and concentration had little effect on the polymer's M_n, $Đ$, or *cis*-selectivity (Table 1, entries 3, 8–12) for Ru-3 catalyzed polymerization.

In contrast, when using cyclometalated Ru-4 and Ru-5 catalysts, the polymerization rate was significantly slower with worse molecular weight control (Table 1, entries 4–7), likely due to the inherently slower initiation rates.[16–19,47,57] Although reducing reaction temperature was detrimental to the monomer conversion, it improved the polymer's M_n, reduced $Đ$, and significantly enhanced *cis*-selectivity (Table 1, entries 4–7). The *cis*-selectivity of P-R4-Ru5 increased from 85% at 25 °C to 93% at 0 °C, possibly because low temperature helps slow down the rate of carbene epimerization.[47] Further investigation by ^{1}H NMR and ^{1}H–^{1}H COSY assignments revealed that the *cis*-selectivity of the less sterically hindered alkenes in P-R4-Ru4 and P-R4-Ru5 increased upon cooling (Fig. S11 and S12). In summary, for Ru-3 catalyzed HT-polymerization of *R*-M4, the solvent has the greatest influence on *cis*-selectivity, whereas for cyclometalated Ru-catalysts, lowering the temperature improves *cis*-selectivity during the HH-polymerization process.

The controlled characteristics of the ROMP of *R*-M4 initiated by Ru-3 were evaluated. M_n increased with the [M] : [I] feeding ratio, and $Đ$ remained below 1.1, confirming the living nature of the polymerization (Fig. 3a). Subsequently, polymerization was conducted with reduced catalyst loading (Table S1). When the feeding ratio was 1000 : 1 (Table S1, entry 1), the polymer's M_n was 490.5 kDa, and $Đ$ was controlled to be 1.08. When the feeding ratio was further increased to 5000 : 1, additional 3-bromopyridine was added to stabilize the active center (Table S1, entries 2–4). The M_n reached up to 1404.1 kDa with a $Đ$ of 1.58. The catalyst molar ratio was successfully reduced to as low as 20 ppm of the monomer ([M] : [I] = 50 000 : 1, Table S1, entry 5), while maintaining a conversion of 99%. However, the formation of ultrahigh molecular weight polymers rendered the product insoluble for GPC analysis. The polymerization of *R*-M4 initiated by Ru-3 was also monitored by *in situ* ^{1}H NMR analysis under a monomer concentration of 0.1 M in chloroform-d with a feeding ratio of 5000 : 1. A conversion of 95% was achieved within only 30 minutes (Fig. 3b). A logarithmic plot of monomer conversion *versus* time was constructed (Fig. S13a), showing a linear relationship between $\ln[M_0/M]$ and time, indicating that the polymerization follows a first-order kinetics reaction. Thus, the Ru-3-catalyzed ROMP of *R*-M4 is rapid and living, which is very similar to the commonly used *exo*-diimide-norbornene ROMP monomers,[10] while *R*-M4 herein gave chiral and isotactic polymers.

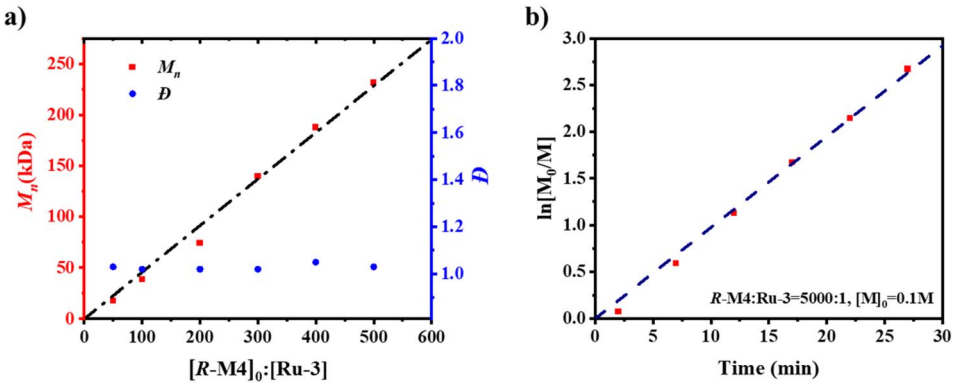

Fig. 3 (a) Plots of P-R4-Ru3's number average molecular weight *versus* the monomer-to-(Ru-3) ratio. (b) First-order kinetic profiles for *R*-M4 obtained by plotting ln[M_0/M] *vs.* time.

Due to the living polymerization of *R*-M4 initiated by Ru-3, block copolymers can be easily synthesized. For example, copolymerization of the *exo*-diimide-norbornene derivative with *R*-M4 gave block copolymers with $Đ = 1.05$ (Fig. S14), no matter which monomer was first added. δ-Pinene, which is another chiral monomer that can undergo regioselective living polymerization using the Ru-3 catalyst,[39] was then copolymerized with *R*-M4 (Fig. 4). Notably, even when δ-pinene, *R*-M4, and Ru-3 were mixed in one pot, the product had a block architecture, likely owing to the significant different polymerization rates. The ^{1}H NMR spectrum was identical to that of the polymer synthesized by sequentially adding δ-pinene and *R*-M4 (Fig. 4c). GPC analysis of both copolymers showed a monomodal distribution with $Đ = 1.28$ (Fig. 4b), and DSC analysis revealed two distinct glass transition temperatures (T_g) (Fig. S15b), further confirming its block copolymer structure. Compared to the sequential addition method for preparing block copolymers, the one-pot approach eliminates the need for additional monomer additions, separations, and purifications, thereby simplifying the process.[4,58] An attempt was also made to copolymerize *R*-M4 with 2,3-dihydrofuran (DHF). It is hypothesized that the high ring strain of *R*-M4 should enable its successful copolymerization to produce a degradable chiral polymer,[59–61] outperforming the low-ring-strain chiral ROMP monomers in

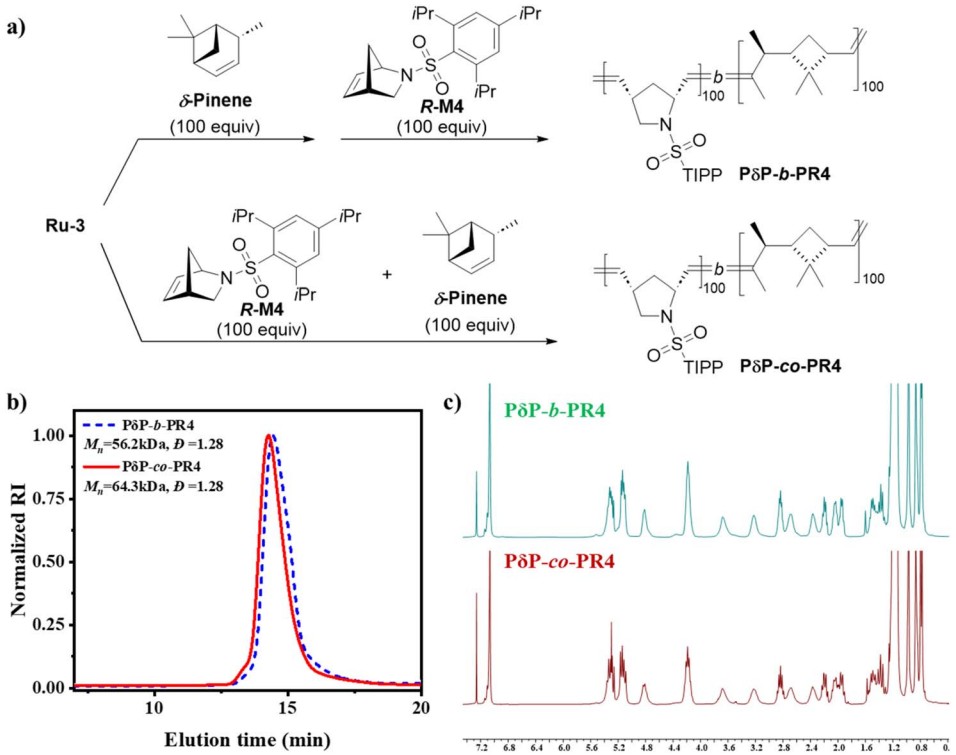

Fig. 4 (a) Synthesis route of sequential addition and one-pot addition block copolymers of δ-pinene and *R*-M4, forming PδP-*b*-PR4 and PδP-*co*-PR4, respectively. (b) GPC traces of PδP-*b*-PR4 and PδP-*co*-PR4. (c) Stacked ^{1}H NMR spectra of PδP-*b*-PR4 and PδP-*co*-PR4.

Table 2 Polymerization and hydrogenation of *R*-M4 or M4 homopolymers[a]

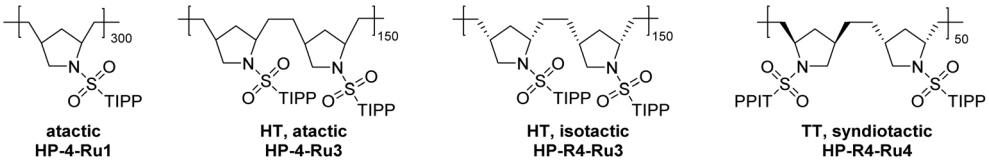

atactic HP-4-Ru1 | HT, atactic HP-4-Ru3 | HT, isotactic HP-R4-Ru3 | TT, syndiotactic HP-R4-Ru4

			Before hydrogenation				After hydrogenation				
Polymers	Initiator	[M] : [I]	M_n/kDa[c]	$Đ$[c]	Yield/%	T_g[e]/°C	M_n/kDa[c]	$Đ$[c]	HD[d]/%	T_g[e]/°C	T_m[e]/°C
HP-4-Ru1	Ru-1	300 : 1	89.8	1.04	99	133.9	90.7	1.12	99	117.6	n. d.
HP-4-Ru3	Ru-3	300 : 1	98.5	1.02	99	135.5	91.3	1.22	97	116.0	n. d.
HP-R4-Ru3	Ru-3	300 : 1	89.9	1.02	99	119.4	102.9	1.11	96	115.5	n. d.
HP-R4-Ru4[b]	Ru-4	100 : 1	581.7	1.66	99	137.5	243.2	1.95	87	285.7	122.4

[a] Reactions were run in dry DCM under a N_2 atmosphere. n. d. = not detected. [b] Solvent is dry THF. [c] Determined by GPC with a RI detector. [d] HD is the degree of hydrogenation of the alkenes in the polymer and determined by ^{1}H NMR. [e] T_g and T_m were determined from the second heating DSC traces.

previous reports.[62] Although the copolymer was successfully prepared with a high molecular weight and high DHF incorporation ratio, the head/tail regioselectivity was completely lost (Fig. S16). After acidic hydrolysis, the resultant fragments were complicated mixtures containing diverse regio- and stereoisomers. This evidence again supports the proposed CEC model for regioselectivity control, as the DHF-derived Fischer carbene is unable to direct selective metathesis with the chiral *R*-M4 monomer.

Subsequently, another chiral monomer, *S*-M4, was synthesized from the other enantiomer of Vince lactam. We aimed to adjust the optical purity of the Ru-3 catalyzed HT-polymer by varying the feeding ratio of *R*-M4 to *S*-M4, aiming to modify the stereoregularity while maintaining excellent HT regioselectivity. As shown in Fig. S17, when both monomers were copolymerized (*R*-M4 : *S*-M4 : Ru-3 = 350 : 150 : 1 or 250 : 250 : 1), the ^{1}H NMR spectra became more complex, indicating a reduction in structural regularity. Nevertheless, compared to the NMR spectrum of P-R4-Ru5, the mixed-feed polymer did not exhibit distinct peaks at 2.98 ppm and 1.98 ppm (highlighted in red in Fig. S17), suggesting that adjusting the optical purity of the monomer affected only the stereoregularity of the polymer, instead of HT regioselectivity. The absence of the representative peak at 60.0 ppm in the ^{13}C NMR of P-4-Ru3 further confirmed that the polymer predominantly contained HT-linked alkenes (Fig. S18). These findings demonstrate that modifying the optical purity of the monomers effectively regulates stereoregularity while preserving regioselectivity.

The impact of regioselectivity on the microstructures and thermal properties was analyzed by X-ray scattering and differential scanning calorimetry (DSC) techniques, respectively, for P-R4-Ru3 (HT selectivity) and P-R4-Ru5 (HH selectivity). Both polymers exhibited amorphous characteristics, with no distinct exothermic crystallization or endothermic melting peaks observed (Fig. S20). The glass transition temperature (T_g) values of P-R4-Ru3 (M_n = 213.2 kDa) and P-R4-Ru5 (M_n = 103.9 kDa) were 128.2 °C and 133.6 °C, respectively. The P-R4-Ru5 polymer had a lower molecular weight yet higher T_g, unambiguously suggesting the positive influence of HH/TT regioselectivity on T_g. In small angle X-ray scattering (SAXS) analysis, the scattering intensity (*I*) *versus* scattering vector (*q*) curves at room temperature (~20 °C) showed no scattering peaks (Fig. S21), further confirming the amorphous structures.

The alkenes present in the main chains of the aforementioned polymers not only influence their fundamental properties, such as thermal stability and mechanical performance,[63] but also constrain molecular chain mobility. This restriction impedes the formation of more ordered structures, thereby limiting the extent to which regioselectivity and tacticity affect the tertiary structure and macroscopic properties of the polymers. To further elucidate the influences of chiral monomers and regioselectivity on polymer properties, we select four representative polymers (P-4-Ru1, P-R4-Ru3, P-R4-Ru4, and P-4-Ru3) for backbone hydrogenation. Specifically, P-4-Ru1 was synthesized *via* the polymerization of the racemic monomer M4 (*R*-M4 : *S*-M4 : Ru-1 = 150 : 150 : 1) initiated by Ru-1, yielding a completely atactic and non-regioselective polymer. After hydrogenation, HP-4-Ru1, HP-4-Ru3, HP-R4-Ru3, and HP-R4-Ru4 were produced, with pre- and post-hydrogenation data shown in Table 2. The hydrogenation degree (HD) of P-R4-Ru4 reached only 87%, likely because the alkene at the head–head connection was too crowded to be efficiently hydrogenated. In the FT-IR spectra of the four hydrogenated polymers (Fig. S22), distinct absorption peaks in the fingerprint region confirm their structural differences.

A comparison of DSC curves before and after hydrogenation (Fig. 5 and S23) further highlights the impact of hydrogenation on the material structure. In the first heating cycle (Fig. S23a), HP-4-Ru1, HP-R4-Ru3, and HP-R4-Ru4 exhibit pronounced endothermic peaks above T_g, with HP-R4-Ru3 displaying the most well-defined peak, suggesting a transition from an amorphous to a semicrystalline state upon hydrogenation. Notably, as regioselectivity shifts from HT to HH, the endothermic peak temperature increases from 241.7 °C (HP-R4-Ru3) to 281.7 °C

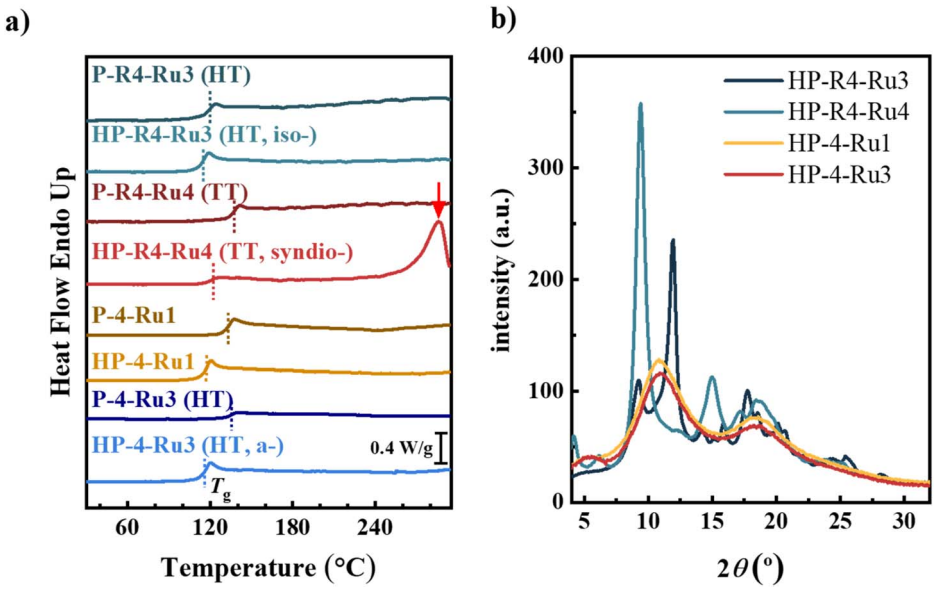

Fig. 5 (a) Comparison of DSC second heating curves before and after hydrogenation of P-R4-Ru3, P-R4-Ru4, P-R4-Ru1, and P-4-Ru3. (b) Comparison of WAXD curves recorded at room temperature (*ca.* 20 °C) of thin films of HP-R4-Ru3, HP-R4-Ru4, HP-4-Ru1, and P-4-Ru3 after hot pressing.

(HP-R4-Ru4). This rise in melting temperature may result from either polymorphism, where different crystal phases formed at different conditions exhibit distinct melting points due to variations in molecular chain arrangement, or differences in lamellar thickness within the same crystal form, with greater lamellar thickness leading to a higher melting temperature according to the Gibbs–Thomson equation. For HP-4-Ru1, which lacks regioselectivity, an endothermic event is observed above 220 °C. However, due to the polymer's thermal decomposition limit, the DSC signals above 300 °C are unable to be measured. In the subsequent cooling cycle (Fig. S23b), only HP-R4-Ru4 exhibits a distinct crystallization exothermic peak (T_c = 207.9 °C), indicating superior crystallization ability compared to the other polymers. This is further confirmed by the second heating curve (Fig. 5a), where HP-R4-Ru4 alone presents a crystallization melting peak (T_m = 285.9 °C). The absence of crystallization exothermic or endothermic peaks in HP-4-Ru1, HP-4-Ru3 and HP-R4-Ru3 (Fig. S23b and 5a) may be attributed to the rapid cooling rate (20 °C min^{-1}), which hinders molecular chain alignment. Consequently, only a limited number of molecular chains are involved in crystallization, resulting in a lower degree of crystallinity characterized by a small peak area and a wider half-height width that is difficult to recognize. Additionally, the second heating curve reveals that hydrogenation lowers the T_g values of these polymers (Table 2).

To clarify whether hydrogenation influences the microstructure of the material, we analyzed the crystalline structure using wide-angle X-ray diffraction (WAXD) and SAXS. The WAXD patterns (Fig. 5b) show multiple diffraction peaks for the regioselective products HP-R4-Ru3 and HP-R4-Ru4, with distinct peak positions, indicating that the differences between HT and HH regioselectivity alter the lattice structure, leading to distinct crystal forms. This also accounts for the variation in crystal melting temperatures observed in the DSC first heating curves (Fig. S23a). Notably, the diffraction peak area of HP-R4-Ru4 represents a larger proportion of the total areas below the curve, suggesting a higher degree of crystallinity. In contrast, HP-4-Ru1 (lacking regioselectivity) and HP-4-Ru3 (HT regioselectivity) exhibited no diffraction peaks in either the WAXD or SAXS curves, underscoring the critical role of the chiral monomer in crystallization. Among the four samples, only HP-R4-Ru3 displayed a scattering peak in the SAXS curve (Fig. S24). The corresponding peak position at $q_{max} \sim 0.06$ $Å^{-1}$ yields a lamellar long period of 10.5 nm, comparable to values typical of polyolefins.[64] Surprisingly, despite its crystalline nature, HP-R4-Ru4 showed no SAXS scattering peak. This may be attributed to differences in its lowest hydrogenation degree (HD of 87% in Table 2, entry 4). The residual alkenes likely disrupt molecular mobility, hindering ordered packing and introducing defects in the crystalline structure, thereby reducing overall crystallinity and preventing SAXS peak formation. Further investigation is required to determine whether hydrogenation degree influences the crystalline structure of polynorbornenes, potentially promoting the formation of small-scale crystal domains and inhibiting larger-scale periodic structures.

In dielectric polymers, dielectric properties arise from the multi-level polarization of molecular chains under an applied electric field.[65–67] At the molecular scale, the dipole moment of a repeating unit is dictated by the structure of its substituents, while at a larger scale, factors such as stereochemical configuration, segmental mobility, and structural regularity influence the net dipole moment.[66,67] For example, Hao demonstrated that vicinal polydichloronorbornene (PDCNB) exhibits distinct dielectric properties due to stereoisomerism, where *exo*-PDCNB shows higher charge–discharge efficiency, while *endo*-PDCNB exhibits greater dielectric breakdown strength.[68] The polymers

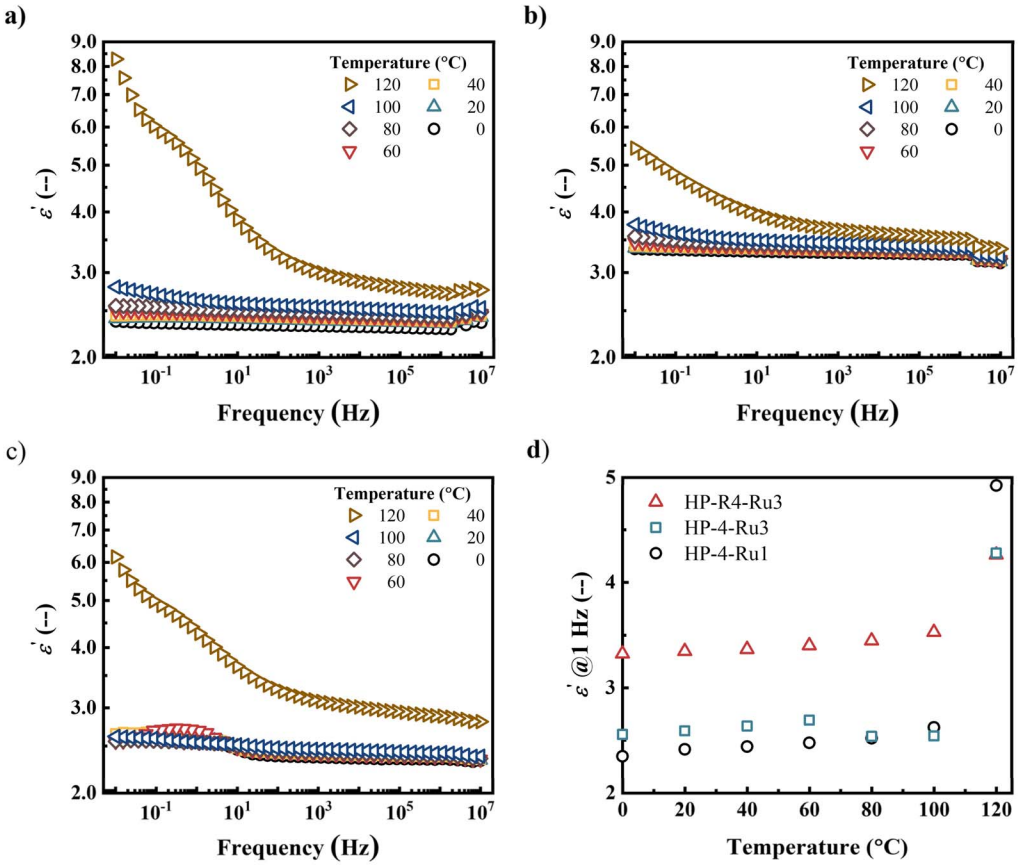

Fig. 6 Variation of ε' with frequency in the temperature range 0–120 °C for thin films of (a) HP-4-Ru1, (b) HP-R4-Ru3, and (c) HP-4-Ru3 after hot pressing. (d) Temperature dependences of ε' obtained at 1 Hz for HP-4-Ru1, HP-R4-Ru3, and HP-4-Ru3.

synthesized in this study enable precise control over regioselectivity through monomer and catalyst selection and form crystalline structures upon hydrogenation. These microstructural variations are expected to influence macroscopic dielectric performance. By comparing dielectric properties across different temperatures, we aim to elucidate the relationship between the polymer microstructure and dielectric behavior.

For variable-temperature dielectric testing, thin films were prepared *via* hot pressing. However, HP-R4-Ru4, with a relatively low hydrogenation degree (~87%), exhibited poor processability, resulting in a rough, uneven surface. Additionally, it turned yellow after hot pressing, likely due to oxidation, which could affect the test results. Therefore, HP-R4-Ru3, possessing HT selectivity and isotactic stereochemistry, was selected as the primary sample, while HP-4-Ru1 and HP-4-Ru3 served as references. The dielectric properties of these three samples were compared across different temperatures (Fig. 6). Fig. 6a and S25a present the variation of the dielectric constant (ε') and dielectric loss (ε'') with frequency for HP-4-Ru1. As temperature increased from 0 °C to 100 °C, ε' rose from 2.34 to 2.62, indicating that even below T_g (T_g ≈ 117.6 °C, Table 2), small-scale molecular motions within the amorphous regions contributed to an enhanced net dipole moment. Above T_g, at 120 °C, whole-chain motion became more significant, leading to pronounced polarization behavior, with ε' at 0.1 Hz increasing to approximately 4.9. In contrast, HP-R4-Ru3, the HT-selective, isotactic, semicrystalline polymer, exhibited a higher initial ε' of 3.32 at 0 °C (Fig. 6b), surpassing both HP-4-Ru1 and HP-4-Ru3. It is noteworthy that HP-4-Ru3 with HT-selective shows a higher ε' than the completely non-selective analogue HP-4-Ru1 within the temperature range of 20–60 °C, demonstrating the effect of regioselectivity on improving ε'. As temperature increased from 0 °C to 100 °C, ε' of HP-R4-Ru3 showed a smaller increase, from 3.32 to 3.52, suggesting a weaker temperature dependence (see Fig. 6d) due to its stable semicrystalline structure, which restricts amorphous segment motion. Above T_g (T_g ≈ 115.5 °C, Table 2), ε' at 0.1 Hz increased modestly to 4.26. These results demonstrate that tuning regioselectivity and tacticity can enhance ε' from approximately 2.34 to 3.32, reaching values suitable for dielectric applications as reported in the literature.[69] Additionally, the high T_g of the norbornene-based polymers ensures that the ε'' peak remains low at temperatures ≤100 °C (Fig. S25), ranging from 6.4×10^{-3} to 1.4×10^{-2}, which is beneficial for extending the material's application.

Conclusion

In summary, we report a simple sulfonamide aza-norbornene derivative (*R*-M4) that can be easily synthesized from commercial chiral Vince lactam. The highly strained monomer exhibits

living ROMP capability and has a broad scope for comonomers, including common norbornene derivatives, δ-pinene, and DHF. More importantly, by using commercial Grubbs' series catalysts and cyclometalated Ru-based catalysts, tunable head/tail regioselectivity is achieved, with the former giving HT and the latter giving HH/TT regioselectivity, respectively. Therefore, the stereochemistry in monomers can be directly transformed into tacticity information in polymers. Detailed experimental and DFT studies suggest the chain-end-control mechanism for the regioselectivity control.

The capability to independently control monomer stereochemistry and ROMP regioselectivity enables us to prepare diverse hydrogenated polymers, including HP-4-Ru1 (no regioselectivity, atactic), HP-4-Ru3 (HT, atactic), HP-R4-Ru3 (HT, isotactic), and HP-R4-Ru4 (HH, syndiotactic). Among the samples, HP-R4-Ru3 and HP-R4-Ru4 exhibited distinct diffraction peaks in WAXD with different crystal forms. Further studies revealed that HP-R4-Ru3, which has better regularity, exhibited a higher dielectric constant compared to the atactic HP-4-Ru1 and HP-4-Ru3, demonstrating that enhancing the regularity of the polymer's microstructure can improve its dielectric properties. We believe that the conveniently prepared chiral monomer with rapid, living, and regioselective ROMP capability would provide a platform to produce diverse chiral polymers.

Author contributions

J. B. performed the synthesis, characterization, analysis, and DFT calculations. Yu W. performed characterization and analysis. Yisong W. and X. W. assisted the synthesis of catalysts and monomers. N. Z. assisted the DFT calculations. All authors contributed to the planning, data analysis and writing of the manuscript.

Conflicts of interest

There are no conflicts to declare.

Data availability

The data supporting this article have been included as part of the supplementary information (SI). Supplementary information: further experimental details, synthetic procedures, characterization data, GPC traces, and copies of NMR spectra. See DOI: https://doi.org/10.1039/d5sc07016c.

Acknowledgements

This work was financially supported by the Strategic Priority Research Program of the Chinese Academy of Sciences (Grant No. XDC0270301). We also thank Prof. Jia Niu (Boston College, USA), Dr Zefeng Zhou (Boston College, USA), Prof. Jian Jiang (ICCAS, China) and Prof. Dingyu Hou (ICCAS, China) for assistance with the DFT calculation.

References

1 J. C. Worch, H. Prydderch, S. Jimaja, P. Bexis, M. L. Becker and A. P. Dove, *Nat. Rev. Chem.*, 2019, **3**, 514–535.
2 C. E. Dingwell and M. A. Hillmyer, *ACS Polym. Au*, 2024, **4**, 208–213.
3 T. M. McGuire, C. Pérale, R. Castaing, G. Kociok-Köhn and A. Buchard, *J. Am. Chem. Soc.*, 2019, **141**, 13301–13305.
4 S. Shin, F. Menk, Y. Kim, J. Lim, K. Char, R. Zentel and T.-L. Choi, *J. Am. Chem. Soc.*, 2018, **140**, 6088–6094.
5 J. Chen, C. Wu, J. Deng, Y. Zhou, F. Liu, K. Shi, P. Jiang and X. Huang, *Adv. Mater.*, 2025, 2417072.
6 S. Sutthasupa, M. Shiotsuki and F. Sanda, *Polym. J.*, 2010, **42**, 905–915.
7 A. Leitgeb, J. Wappel and C. Slugovc, *Polymer*, 2010, **51**, 2927–2946.
8 R. Szweda, *Prog. Polym. Sci.*, 2023, **145**, 101737.
9 Y. Li, S. M. Kang, G. Shi, Y. F. Chen, B. W. Li, J. Zhang and X. H. Wan, *Chin. J. Polym. Sci.*, 2025, **43**, 61–69.
10 C. W. Bielawski and R. H. Grubbs, *Prog. Polym. Sci.*, 2007, **32**, 1–29.
11 K. Nomura and M. M. Abdellatif, *Polymer*, 2010, **51**, 1861–1881.
12 A. F. M. Kilbinger, *Synlett*, 2019, **30**, 2051–2057.
13 X. Wang, Y. Wen, Y. Wang, W. Li, X. Lu and W. You, *CCS Chem.*, 2024, **6**, 2305–2317.
14 J. D. Feist and Y. Xia, *J. Am. Chem. Soc.*, 2020, **142**, 1186–1189.
15 M. E. Hansen and Y. Xia, *ACS Macro Lett.*, 2025, **14**, 1492–1496.
16 I. Mandal and A. F. M. Kilbinger, *J. Am. Chem. Soc.*, 2024, **146**, 32072–32079.
17 T. W. Hsu, C. Kim and Q. Michaudel, *J. Am. Chem. Soc.*, 2020, **142**, 11983–11987.
18 T. W. Hsu, S. J. Kempel and Q. Michaudel, *J. Polym Sci.*, 2022, **60**, 569–578.
19 J. L. Nicholson, A. C. Gravet and Q. Michaudel, *Faraday Discuss.*, 2025, DOI: 10.1039/D5FD00067J.
20 R. R. Schrock, *Acc. Chem. Res.*, 2014, **47**, 2457–2466.
21 M. M. Flook, V. W. L. Ng and R. R. Schrock, *J. Am. Chem. Soc.*, 2011, **133**, 1784–1786.
22 J. Hyvl, B. Autenrieth and R. R. Schrock, *Macromolecules*, 2015, **48**, 3148–3152.
23 L. E. Rosebrugh, T. S. Ahmed, V. M. Marx, J. Hartung, P. Liu, J. G. López, K. N. Houk and R. H. Grubbs, *J. Am. Chem. Soc.*, 2016, **138**, 1394–1405.
24 K. J. Ivin, A. M. Kenwright, E. Khosravi and J. G. Hamilton, *Macromol. Chem. Phys.*, 2001, **202**, 3624–3633.
25 B. Ai-Samak, V. Amir-Ebrahimi, A. G. Carvill, J. G. Hamilton and J. J. Rooney, *Polym. Int.*, 1996, **41**, 85–92.
26 L. Delaude, A. Demonceau and A. F. Noels, *Macromolecules*, 1999, **32**, 2091–2103.
27 L. Delaude, A. Demonceau and A. F. Noels, *Macromolecules*, 2003, **36**, 1446–1456.
28 T. Sunaga, K. J. Ivin, G. E. Hofmeister, J. H. Oskam and R. R. Schrock, *Macromolecules*, 1994, **27**, 4043–4050.

29 R. O'Dell, D. H. McConville, G. E. Hofmeister and R. R. Schrock, *J. Am. Chem. Soc.*, 1994, **116**, 3414–3423.
30 L. E. Rosebrugh, V. M. Marx, B. K. Keitz and R. H. Grubbs, *J. Am. Chem. Soc.*, 2013, **135**, 10032–10035.
31 R. R. Schrock, *Dalton Trans.*, 2011, **40**, 7484–7495.
32 B. F. Straub, *Adv. Synth. Catal.*, 2007, **349**, 204–214.
33 S. E. Blosch, S. J. Scannelli, M. Alaboalirat and J. B. Matson, *Macromolecules*, 2022, **55**, 4200–4227.
34 S. Varlas, S. B. Lawrenson, L. A. Arkinstall, R. K. O'Reilly and J. C. Foster, *Prog. Polym. Sci.*, 2020, **107**, 101278.
35 J. Xu and N. Hadjichristidis, *Prog. Polym. Sci.*, 2023, **139**, 101656.
36 J. Zhang, M. E. Matta, H. Martinez and M. A. Hillmyer, *Macromolecules*, 2013, **46**, 2535–2543.
37 G. A. Guillory, S. F. Marxsen, R. G. Alamo and J. G. Kennemur, *Macromolecules*, 2022, **55**, 6841–6851.
38 K. Fukushima, K. Matsuzaki, M. Oji, Y. Higuchi, G. Watanabe, Y. Suzuki, M. Kikuchi, N. Fujimura, N. Shimokawa, H. Ito, T. Kato, S. Kawaguchi and M. Tanaka, *Macromolecules*, 2022, **55**, 15–25.
39 M. R. Yarolimek, H. R. Bookbinder, B. M. Coia and J. G. Kennemur, *ACS Macro Lett.*, 2021, **10**, 760–766.
40 R. Singh and R. Vince, *Chem. Rev.*, 2012, **112**, 4642–4686.
41 M. J. Benedikter, G. Frater and M. R. Buchmeiser, *Macromolecules*, 2018, **51**, 2276–2282.
42 M. J. L. Tschan, R. M. Gauvin and C. M. Thomas, *Chem. Soc. Rev.*, 2021, **50**, 13587–13608.
43 A. Bhaumik, G. I. Peterson, C. Kang and T. L. Choi, *J. Am. Chem. Soc.*, 2019, **141**, 12207–12211.
44 S. Kobayashi, L. M. Pitet and M. A. Hillmyer, *J. Am. Chem. Soc.*, 2011, **133**, 5794–5797.
45 S. Brits, W. J. Neary, G. Palui and J. G. Kennemur, *Polym. Chem.*, 2018, **9**, 1719–1727.
46 Y. Wang, Z. Zhang and Y. Xu, *Macromolecules*, 2023, **56**, 9138–9145.
47 B. K. Keitz, A. Fedorov and R. H. Grubbs, *J. Am. Chem. Soc.*, 2012, **134**, 2040–2043.
48 M. B. Herbert and R. H. Grubbs, *Angew. Chem., Int. Ed.*, 2015, **54**, 5018–5024.
49 Q. Michaudel, S. J. Kempel, T. W. Hsu and J. N. deGruyter, in *Comprehensive Organometallic Chemistry IV*, ed. G. Parkin, K. Meyer and D. O'hare, Elsevier, Oxford, 2022, pp. 265–338.
50 A. G. Kruger, S. D. Brucks, T. Yan, G. Cárcarmo-Oyarce, Y. Wei, D. H. Wen, D. R. Carvalho, M. J. A. Hore, K. Ribbeck, R. R. Schrock and L. L. Kiessling, *ACS Cent. Sci.*, 2021, **7**, 624–630.
51 S. Takebayashi, M. A. Iron, M. Feller, O. Rivada-Wheelaghan, G. Leitus, Y. Diskin-Posner, L. J. W. Shimon, L. Avram, R. Carmieli, S. G. Wolf, I. Cohen-Ofri, R. A. Sanguramath, R. Shenhar, M. Eisen and D. Milstein, *Nat. Catal.*, 2022, **5**, 494–502.
52 D. Chriti, G. Raptopoulos, B. Brandenburg and P. Paraskevopoulou, *Polymers*, 2020, **12**, 1033.
53 Z. Zhou, Q. Pham, G. J. Giardino, A. Chatterjee and J. Niu, *J. Am. Chem. Soc.*, 2025, **147**, 16754–16759.
54 H. Miyazaki, M. B. Herbert, P. Liu, X. Dong, X. Xu, B. K. Keitz, T. Ung, G. Mkrtumyan, K. N. Houk and R. H. Grubbs, *J. Am. Chem. Soc.*, 2013, **135**, 5848–5858.
55 Y. Xu, J. J. Wong, A. E. Samkian, J. H. Ko, S. Chen, K. N. Houk and R. H. Grubbs, *J. Am. Chem. Soc.*, 2020, **142**, 20987–20993.
56 L. Goerigk, A. Hansen, C. Bauer, S. Ehrlich, A. Najibi and S. Grimme, *Phys. Chem. Chem. Phys.*, 2017, **19**, 32184–32215.
57 B. K. Keitz, K. Endo, P. R. Patel, M. B. Herbert and R. H. Grubbs, *J. Am. Chem. Soc.*, 2012, **134**, 693–699.
58 X. Fu, X. Lin, M. Wang, Z. Ding, G. Ma, B. Wang and Y. Li, *Macromolecules*, 2024, **57**, 5691–5701.
59 J. D. Feist, D. C. Lee and Y. Xia, *Nat. Chem.*, 2022, **14**, 53–58.
60 T. An, H. Ryu and T. Choi, *Angew. Chem., Int. Ed.*, 2023, **62**, e202309632.
61 X. Sui and W. R. Gutekunst, *ACS Macro Lett.*, 2022, **11**, 630–635.
62 F. A. Starvaggi, B. A. Suslick and Y. Xia, *ACS Macro Lett.*, 2024, 296–301.
63 C. Derosa and F. Auriemma, *Prog. Polym. Sci.*, 2006, **31**, 145–237.
64 C. Qian, Y. Zhao, Y. Wang, C. Zhang and D. Wang, *Polymer*, 2021, **236**, 124310.
65 B. Zhong, Y. Zhang, W. You and Y. Wang, *RSC Appl. Polym.*, 2025, **3**, 97–110.
66 L. Zhu, *J. Phys. Chem. Lett.*, 2014, **5**, 3677–3687.
67 S. Wang, C. Yang, X. Li, H. Jia, S. Liu, X. Liu, T. Minari and Q. Sun, *J. Mater. Chem. C*, 2022, **10**, 6196–6221.
68 J. Hao, S. Shukla, R. Gurnani, M. Mukherjee, H. Sahu, A. Khomane, P. Aklujkar, M. Desai, C. Wu, R. Ramprasad, G. Sotzing and Y. Cao, *Adv. Mater.*, 2025, 2417625.
69 X. J. Liu, M. S. Zheng, G. Chen, Z. M. Dang and J. W. Zha, *Energy Environ. Sci.*, 2022, **15**, 56–81.